



Effect of Fe Intermetallics on Microstructure and Properties of Al-7Si Alloys

JAMES MATHEW,¹ GUILLAUME REMY,¹ MARK A. WILLIAMS,¹
FENGZAI TANG,¹ and PRAKASH SRIRANGAM^{1,2}

1.—Warwick Manufacturing Group, University of Warwick, Coventry CV4 7AL, UK.
2.—e-mail: p.srirangam@warwick.ac.uk

The present work deals with the effect of iron intermetallics on the microstructure and mechanical properties of Al-7% Si alloys. Two different iron additions were made, 0.6% Fe and 2% Fe, to study the effect of iron intermetallics on Al-Si alloys. Microstructure property correlations were carried out using SEM-EDS and tensile testing of alloys. Microstructure results show that the rise in iron content significantly increased the average size, thickness and number of intermetallic particles in the alloys. Nano-indentation study shows that the iron intermetallics are too brittle compared with the primary aluminium. Moreover, the hardness and Young's modulus of iron intermetallics are higher than those of primary aluminium. Tensile test results show that there is no significant difference in strength levels between Al-7%Si and Al-7Si-0.6Fe alloys. However, an increase in iron from 0.6% to 2% resulted in a significant decrease in tensile strength and elongation of the alloys. Two-dimensional SEM studies suggest that the increased number of needle-shaped β -phase intermetallic particles formed because of increased amounts of Fe could be the reason for early failure of the alloy. To further understand the early failure of iron-containing alloys, the fractured tensile specimens were studied using the 3D x-ray tomography technique. XCT results show that the failure in tensile testing of 2% Fe alloy was not mainly due to breaking of brittle β -phase intermetallic particles, but due to the morphology and particle-matrix interface debonding. XCT shows that the needle-shaped particles are long, sharp-edged platelets in 3D, which act as stress raisers for crack initiation and propagation along the interphase.

INTRODUCTION

Recycling of aluminium and aluminium alloys is a topic of interest in automotive and aerospace industries because of the economic and environmental benefits associated with it.¹ Most aluminium alloy scrap for recycling is generated from the automotive and beverage industries.² Al alloy scrap for recycling usually contains impurity elements such as iron, which leads to casting defects and eventually deteriorates the mechanical properties of alloys.² Al has limited solubility of iron and hence forms intermetallic compounds such as β - and α -phase compounds during solidification of the alloy.³ Iron levels can reach 2 wt.% at about 700°C melt temperature and up to 5% for holding at 800°C melt

temperature. The major intermetallic phases formed in Al-Si alloys with iron are α -Al₈Fe₂Si and β -Al₅FeSi. The α -Al₈Fe₂Si phase is hexagonal shaped, and the β -Al₅FeSi phase has a monoclinic/orthorhombic structure.⁴ β -phase intermetallic particles have been considered more harmful in deteriorating the mechanical properties of aluminium alloys.⁴ The other β phases identified in Al-Si alloys are Al₃FeSi₂, Al₄FeSi, Al₉Fe₂Si₂, β -Al₅FeSi, Al₅FeSi, β -Al_{4.5}FeSi and Fe₂SiAl₅.⁵ The size, shape and chemical composition of these iron intermetallics vary widely among each other and hence can significantly affect the mechanical properties of the alloy. The α -type intermetallics have a Chinese script-like morphology, whereas β phase generally has a needle-like morphology.⁴

However, three-dimensional analysis later showed that the β phase is platelet shaped, but was misinterpreted as needle shaped in 2D observations.⁶ The β -phase intermetallic particles were considered more harmful in deteriorating the mechanical properties of aluminium alloys.⁷ Several studies have been carried out to understand the effect of intermetallics on the mechanical properties of Al-Si alloys.^{8–11} However, most of these studies show the effect of intermetallics on mechanical properties only by considering 2D microstructural observations.

Therefore, it is essential to study the effect of iron intermetallics on the mechanical properties of Al-Si alloys with 3D investigation of the tensile samples to understand the exact early failure of these alloys with increased levels of iron in recycled alloys. In this work, we present the effect of iron content on the microstructure and mechanical properties of Al-7 wt.% Si alloy and Al-7 wt.% Si-2 wt.% Fe alloy using high-resolution electron microscopy imaging and 3D x-ray computed tomography (XCT) investigation.

EXPERIMENTAL DETAILS

Alloy Preparation

Al-7 wt.% Si alloy was prepared by melting 99.9% purity aluminium (Avon metals Ltd., UK) in a clay graphite crucible using a Carbolite high-temperature chamber furnace and then adding Al-20 wt.% Si master alloy to the molten alloy. The mixture was stirred intermittently to ensure proper mixing. After keeping the mixture at 740°C for 10 min to ensure the master alloy was completely dissolved in the melt, the mixture was then poured into a clay graphite cylindrical mould (55 mm diameter, 97 mm deep). A portion of the Al-7 wt.% Si alloy was then re-melted to prepare the Al-7Si-2Fe alloy. When the Al-7 wt.% Si alloy was in a molten state, the Al-10 wt.% Fe master alloy (ACI Alloys) was added in respective proportions to the melt and stirred well to dissolve the Al-10 wt.% Fe completely in the melt. After keeping the melt at 740°C for 10 min, the molten metal was poured into the same mould.

Microstructural Characterisation

Microstructural studies of Al-7Si alloy and Al-7Si-2Fe alloys were carried out using a scanning electron microscope (SEM) after polishing the samples using standard metallographic procedures. Elemental distribution maps were captured using a Zeiss Sigma SMT AG instrument coupled with an energy-dispersive x-ray spectrometer (EDS).

Nano-indentation

Nano-indentation tests were performed in a nano-indentation instrument (Micro Materials) with a standard Berkovich indenter (included angle,

142.3°), which constantly measures force and displacement as the indentation advances. The sample was prepared flat and finely polished to avoid surface roughness effects during indentation. The indentations (12 each) were made from both particle and primary aluminium with a maximum load of 5 mN. The load was applied in 20 s and kept at maximum load for 6 s (dwell) and unloaded in 20 s. Each indentation was separated by 25 μ m. The detailed test procedure can be found elsewhere.^{12,13} The peak indentation depth (h_{\max}) is the maximum displacement of the indenter from its initial position at peak load (P_{\max}). It includes both elastic and plastic deformation. Nevertheless, the material elastically recovers its shape partially when the indenter is unloaded.¹⁴ From these data, elastic displacements are measured for calculating the elastic modulus, E. The hardness, H, can be calculated by removing this elastic contribution from the total displacement.

The hardness (H) can be calculated as:

$$H = \frac{P_{\max}}{A} \quad (1)$$

where P_{\max} is the peak load and A is the projected area of contact between the indenter and the sample.^{13,15}

Mechanical Property Characterisation

Cylindrical tensile samples were prepared using a CNC lathe according to the dimensions specified in ASTM E-8M.¹⁶ Tensile properties were evaluated using a 100-kN universal tensile testing machine (Instron model 5800R) at a constant crosshead speed of 2 mm/min. The measurements were taken with five samples for each condition, and the average value was used in determining the tensile properties of the alloys. The fracture surface was then studied using a Zeiss Sigma SMT AG instrument.

X-ray Computed Tomography (XCT)

The tensile samples were scanned before and after the test using the Zeiss Versa at CiMat, WMG, University of Warwick, UK. Samples were prepared as 5-mm-diameter cylinders and scanned under the conditions given in the Table I. To reach the best resolution possible, a 0.4 \times flat panel was used as

Table I. X-ray tomography scanning parameters

Scanning condition	Zeiss Versa
Voltage (kV)	80
Current (μ A)	87
Number of projections	1601
Filtration	LE4
Voxel size (μ m)	3.67

detector. The detector is composed of 2048×2048 pixels resulting in $3.67\text{-}\mu\text{m}$ resolution. The raw data were reconstructed using the Zeiss reconstruction software, which uses a filtered back projection (FBP) algorithm creating a stack of DICOM images. The stack can then be used for analysis with Avizo 9.4.0 (FEI, USA; <http://www.fei.com/software/avizo3d>).

RESULTS

Figure 1 shows the SEM images of Al-7Si, Al-7Si-0.6Fe and Al-7Si-2Fe alloys. These images show the 2D morphology of the silicon and iron intermetallic particles. The white particles in the microstructure are iron intermetallics and the bright grey particles are silicon flakes. The Al-7 wt.% Si-0.6 wt.% Fe microstructure (Fig. 1b) and Al-7 wt.% Si-2 wt.% Fe microstructure (Fig. 1c) show the iron intermetallic particles in the aluminium matrix. Al-7Si-2Fe has many intermetallics, whereas the Al-7Si-0.6Fe alloy is found to have only a few. The intermetallics were observed to be long and needle shaped, and they were uniformly distributed in the matrix of the Al-7Si-2Fe alloy. This shows that the increase in iron content from 0.6% Fe to 2% Fe resulted in a significant increase in the volume fraction of iron intermetallics in the alloy.

Figure 2 shows the SEM-EDS elemental analysis of the Al-7 wt.% Si alloy, Al-7 wt.% Si-0.6 wt.% Fe and Al-7 wt.% Si-2 wt.% Fe. In Fig. 2, green represents the aluminium matrix, yellow the silicon phase and blue the iron particles in the alloy. The EDS images clearly distinguish the aluminium, silicon and intermetallic phases. As shown in Fig. 2, the iron intermetallics have a needle-shaped morphology. The iron intermetallics are thicker and denser in number in the Al-7Si-2Fe alloy (Fig. 2c) compared with the Al-7Si-0.6Fe alloy (Fig. 2b). Also, it was observed that eutectic silicon is modified and finely distributed in the Al-7Si-0.6Fe alloy compared with the Al-7Si-2Fe alloy and Al-7 wt.% Si alloy (yellow coloured particles in Fig. 2a–c). This is due to the heterogeneous nucleation of the silicon phases on β -iron intermetallic phases,^{17,18} which are predominant at critical Fe content (Fe_{crit}), which is ~ 0.5 for Al-7% Si alloy.⁴

Taylor et al.¹⁸ explained this mechanism based on a critical Fe concentration (Fe_{crit}). At the critical iron content, the alloy will solidify in two stages where the ternary AlSi- β eutectic platelets form first and the eutectic silicon cells nucleate only on small ternary AlSi- β platelets, whereas, at subcritical iron contents ($< Fe_{crit}$) and supercritical iron contents ($> Fe_{crit}$), the alloy solidifies in more than two stages. At subcritical iron contents ($< Fe_{crit}$), the large silicon eutectic cells nucleate themselves and grow before the nucleation of smaller eutectic cells on the AlSi- β ternary platelets. At supercritical iron contents ($> Fe_{crit}$), large eutectic silicon cells nucleate on the already formed binary Al- β platelets before the nucleation of small eutectic cells on the ternary AlSi- β ternary platelets. The refinement of silicon particles improves the mechanical properties of aluminium silicon alloys. Hegde et al.¹⁹ reported a noticeable improvement in elongation and strength upon modification of silicon phase in aluminium silicon alloys.

The hardness and elastic modulus of iron intermetallics, silicon-rich areas and aluminium in the Al-7Si-2Fe alloy were determined from their respective loading-unloading curve using the method proposed by Oliver and Pharr.^{12,20} To minimise the indentation size effects, a $25\text{-}\mu\text{m}$ interval between each indentation was used.^{21,22} Figure 3 shows the loading-unloading curve of different area/particles in the Al-7Si-2Fe alloy from which the hardness and elastic modulus were measured. The indentations on the iron intermetallic particles (red colour) attain a maximum depth of ~ 150 nm, whereas indentations on the aluminium (blue colour) attain a maximum depth of ~ 550 nm. The displacement on constant load of 5 mN also shows this increasing nature (top peak of the curves). This indicates that the iron intermetallics are less ductile/more brittle than aluminium. The hardness and Young's modulus of the iron intermetallic particle are significantly higher than those of aluminium and silicon flake-rich areas. The average nano-hardness of the primary aluminium is 1.05 ± 0.01 GPa and of iron intermetallics is 9.53 ± 0.18 GPa, whereas the average Young's modulus is 102.78 ± 1.97 GPa and 174.30 ± 11.28 GPa, respectively. This is almost

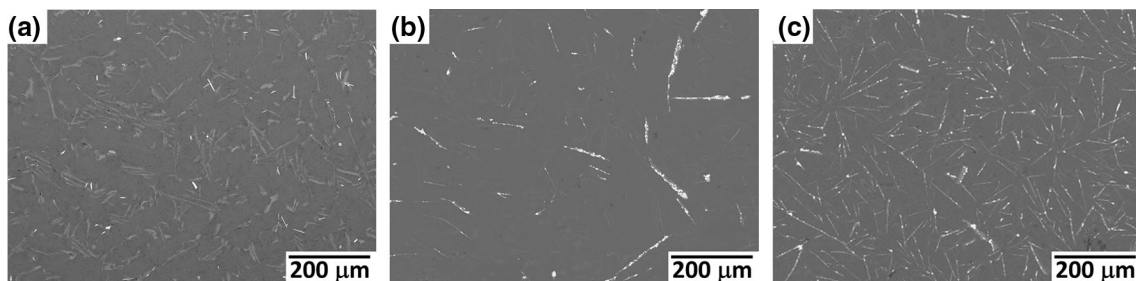


Fig. 1. SEM images of (a) Al-7Si, (b) Al-7Si-0.6Fe and (c) Al-7Si-2Fe alloys.

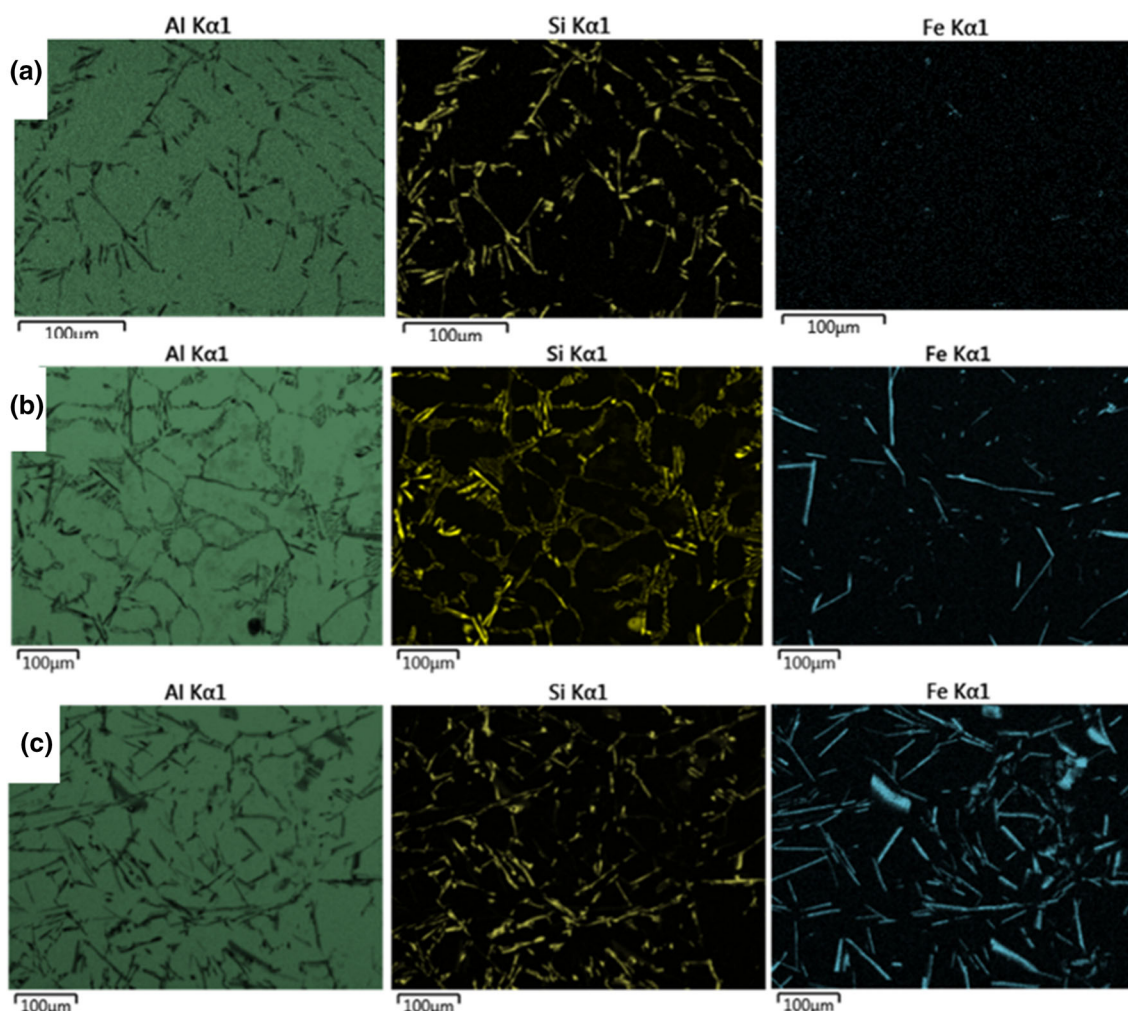


Fig. 2. SEM-EDS elemental mapping of (a) Al-7% Si alloy, (b) Al-7% Si-0.6% Fe alloy and (c) Al-7% Si-2% Fe alloy.

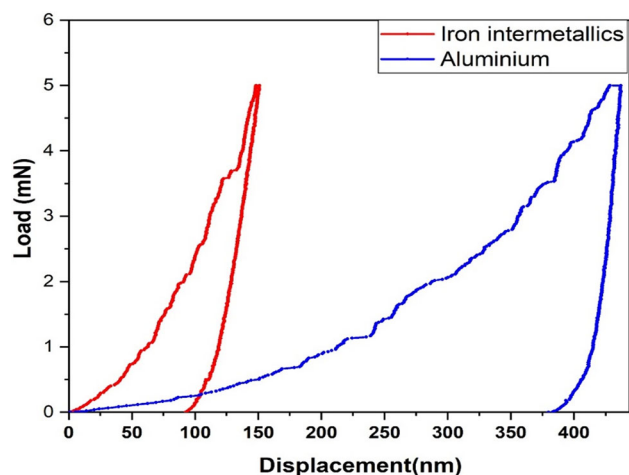


Fig. 3. Loading-unloading curve of Al-7Si-2Fe alloy.

consistent with the literature from Chen et al.¹¹ who reported a hardness of 10.82 GPa and 175.32 GPa for iron intermetallics in the AlSiFeMn alloy by nano-indentation. The hardness and Young's modulus obtained for the primary

aluminium are higher than those for pure aluminium (0.7 GPa and 70 GPa, respectively). Youn et al.²³ reported an average elastic modulus of 77 GPa for primary aluminium in the Al-Si alloy and an average nano-hardness of 1.0 GPa. However, the average elastic modulus obtained for primary aluminium was higher than that in the literature. This could be due to the presence of silicon particles in the alloy.

The tensile properties of Al-7% Si, Al-7% Si-0.6% Fe and Al-7% Si-2% Fe alloys were measured to determine the effect of intermetallics on the mechanical properties of Al-7Si alloys. Figure 4a shows the load versus elongation of the Al-7Si alloy (red colour), Al-7Si-0.6Fe (blue colour) alloy and Al-7Si-2Fe (green colour) alloy. The maximum load capacity for the Al-7Si alloy was found to be 2686.60 ± 159.91 N with maximum elongation of 1.25 ± 0.12 mm, whereas for Al-7Si-2Fe alloy the load was 1991.64 ± 220.12 N and the elongation was 0.51741 ± 0.08 mm, respectively. This shows that increasing the Fe content to 2% resulted in a decrease in the load-bearing capacity by 25%

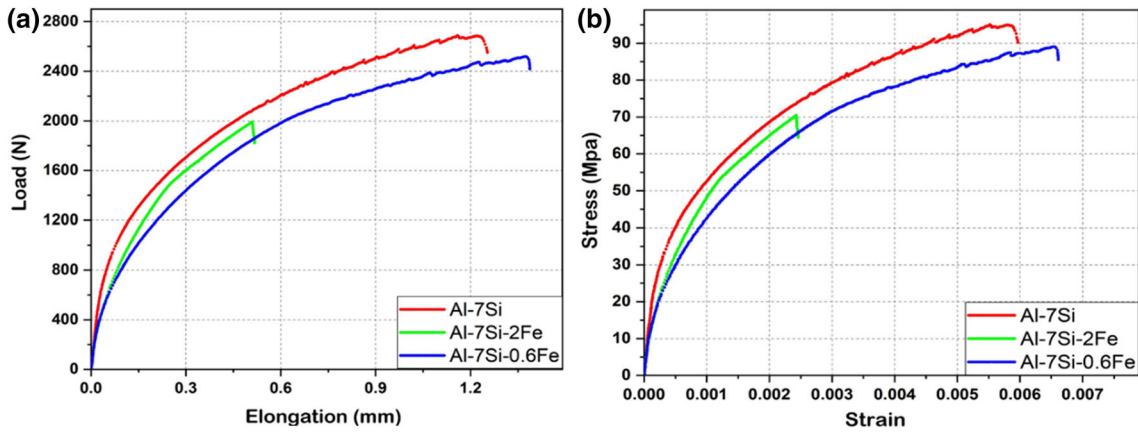


Fig. 4. Tensile properties: (a) load versus elongation; (b) tensile stress versus strain.

compared with the Al-7% Si alloy. Also, the maximum elongation dropped by 58% with 2% iron addition to the Al-7% Si alloy. However, the addition of 0.6% iron results in a maximum load capacity of 2518.18 ± 42.67 N and a maximum elongation of 1.39 ± 0.19 mm. This shows an increase in the elongation by 10.67% even though the maximum load capacity/strength is decreased by 6.26%. This difference in elongation may be due to the critical iron content (Fe_{crit}) of the Al-7Si-0.6Fe alloy, which refines the silicon particles or the casting defects (porosity) or their combined effect,^{4,18} whereas the higher fraction of iron intermetallics formed on addition of 2 wt.% Fe significantly deteriorates the mechanical properties of the alloy. Thus, this indicates that, even though the iron intermetallics form with 0.6% Fe, their effect on deteriorating the mechanical properties of the alloy is negligible. These observations can be correlated with the critical iron content values of Al-7Si alloys.^{4,24} Narayanan et al.⁴ reported that when the iron content exceeds 0.7%, the intermetallic compounds tend to form as large platelets, which deteriorate the mechanical properties of the alloy.

Figure 4b shows the tensile stress versus strain curve of the Al-7Si alloy (red colour), Al-7Si-0.6Fe (blue colour) alloy and Al-7Si-2Fe (green colour) alloy. The maximum tensile stress for the Al-7Si alloy is 95.01 ± 5.65 MPa, for the Al-7Si-0.6 Fe alloy is 89.06 ± 1.14 MPa and for the Al-7Si-2Fe alloy is 70.43 ± 7.78 MPa. This shows that the increase in iron levels to 2% resulted in a significant drop in the tensile properties of the alloy. However, similar observations of a reduction of the mechanical properties on addition of Fe were reported for other Al-Si based alloys with iron intermetallics.^{25–27} Sacinti et al.²⁶ studied the effect of iron intermetallics on the mechanical properties of Al-7Si-0.3 Mg and reported that the size of the β platelets was doubled when the Fe content doubled, which eventually led to a three-fold reduction in the

elongation value. Ravi et al.²⁷ also concluded that the higher the Fe content in the alloy is, the lower the mechanical properties of the alloy.

Figure 5 shows the fracture surface of the tensile samples of Al-7Si and Al-7Si-2Fe alloys. The aluminium dendrites are visible in both cases with no significant damage of the primary aluminium in the alloy. The intermetallic particles are clearly visible in Al-7Si-2Fe alloys (Fig. 5b). Figure 5b shows the third dimension of the needle-shaped particles. The particles, which were previously reported as needles in SEM images, are actually thin platelets in 3D, as shown in Fig. 5b. The platelet-shaped particles with sharp edges project out from the fracture surface without any rupture. This sharp-edged platelet shape increases the stress concentration factor, thereby resulting in the formation of cracks at the particle-matrix interface in the high iron-containing alloy.^{28,29} This shows that during tensile loading the intermetallic particles were pulled out along the interfacial boundary between the intermetallics and aluminium matrix without causing any destruction of the brittle intermetallic particles. Also, this observation suggests that the early failure of the Al-7Si-2Fe alloy particularly results from the intermetallic particle pull-out, which in turn helps in the crack propagation along the particle edges. Wang et al.¹⁰ reported that the large intermetallic particles enhance the crack propagation more than the fragmented intermetallic particles in the alloy.

Furthermore, the fracture surfaces were studied using 3D x-ray tomography to better understand the early failure of iron-containing alloys during tensile testing. Figure 6 shows the fracture study of the tensile samples of Al-7Si-2Fe alloys using 2D orthogonal slices ($3.5 \text{ mm} \times 3.5 \text{ mm}$) from XCT scans. The 2D slices from XCT scans were studied using Avizo 9.8 software. Since the cylindrical tensile samples with 6 mm diameter are not easy to analyse because of varying contrast along the cross section, a cuboid subvolume with $3.5 \text{ mm} \times$

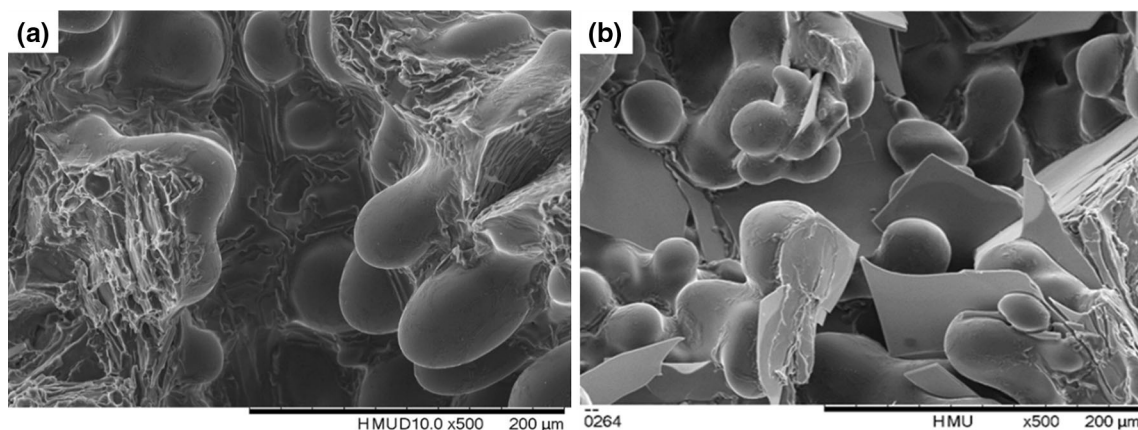


Fig. 5. Fracture surface of (a) Al-7Si and (b) Al-7Si-2Fe alloys.

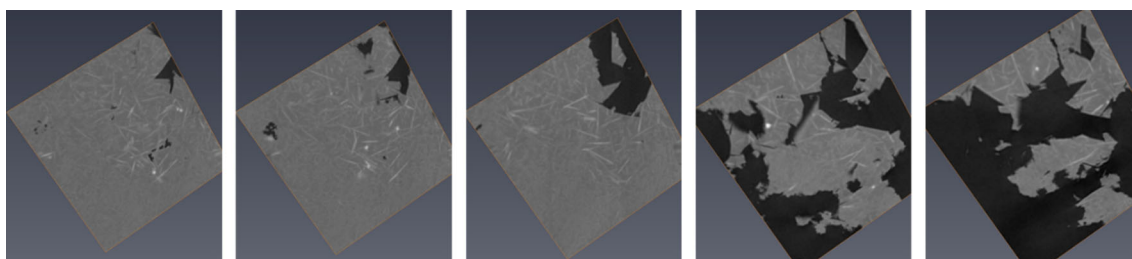


Fig. 6. 2D slices showing the crack propagation (top to centre of the fracture region).

3.5 mm cross section was made out of the 3D reconstructed cylindrical sample. The orthogonal slices from the top to centre of the fracture region are as shown in the figure from left to right, respectively. The images show that that the crack is along the particles (white coloured). Almost all of the cracks are sharp edged, demonstrating a fracture along the sharp-edged intermetallic particle boundaries. The results suggest that the intermetallic particles are not fractured on extension, but act as stress risers for initiation of the crack. The propagation of the crack is through the interface boundary of the particles and aluminium matrix. Since the particles are elongated and interconnected with sharp edges, crack can easily propagate from one end to the other.

Figure 7a shows the 3D reconstructed image of the Al-7Si-2 wt.%Fe alloy. In Fig. 7, blue colour represents the porosity, while red and white represent the iron intermetallics and aluminium matrix, respectively. Figure 7b shows the 3D reconstructed image of Al-7% Si-2%Fe alloy without porosities. As shown in Fig. 7b, $\text{Al}_{13}\text{Fe}_4$ iron intermetallics were found to have a platelet morphology in 3D compared with their appearance as needles in 2D images. The needle-type morphology that appears in 2D has a third dimension, and the particles were observed to have a thin platelet shape with very sharp edges. The failure crack (thick dense blue) was formed in an area in the sample where the iron intermetallic presence was higher (Fig. 7a). The porosity including the region of failure has been removed in Fig. 7b

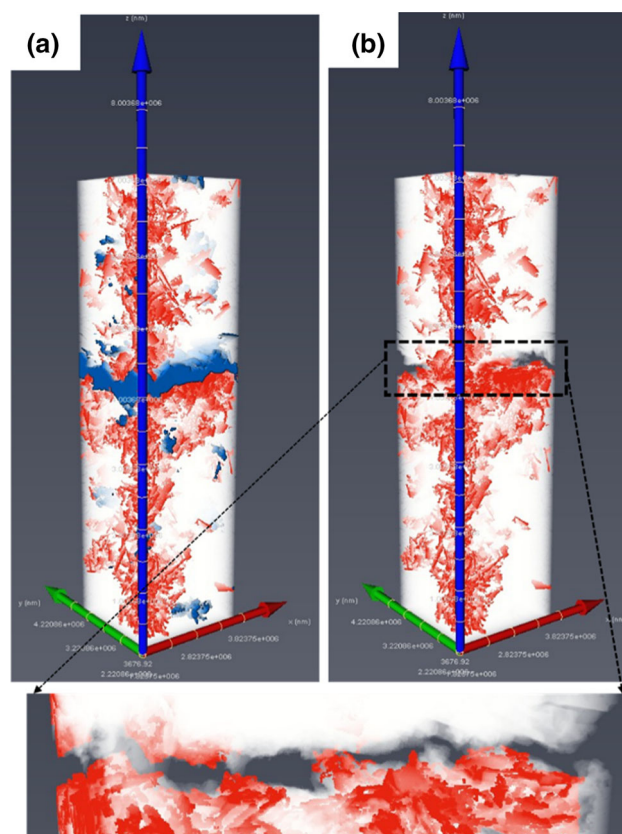


Fig. 7. 3D reconstructed XCT images (a) showing porosity (blue colour) as well as particles (red colour) in the Al matrix (white) and (b) showing particles (red colour) in the Al matrix (white) (Color figure online).

for better observation of the fracture area. Figure 7b clearly shows that the fracture has occurred in an area where there is a higher number of intermetallic particles. Also, the fracture area in the Fig. 7b (zoomed in) shows that the crack propagated along the surface of the intermetallics without rupture and fracture of the particles. This indicates that the early failure of the iron-containing alloy is not due to the brittleness of the intermetallic particles, but due to the morphology of the intermetallic particles. Yi et al.²⁸ reported crack formation and propagation along the interfaces by debonding of Fe-rich intermetallic and Si particles from the matrix in the alloy. A similar observation was made by Gall et al.²⁹ in which the fatigue cracks debonded almost all of the silicon particles in the Al-Si alloys. Also, the fracture occurred at the elongated particles, which have a major axis perpendicular to the crack plane.

The present study using the 3D XCT technique clearly shows that adding 2 wt.% iron to Al-7Si results in an increased volume fraction of iron intermetallic formation, which results in a decrease in the mechanical properties of the alloys. Nano-indentation studies show that the iron intermetallic particles are hard and brittle compared with the primary aluminium. The 3D visualisation of intermetallics not only shows the morphology of intermetallics, but is also useful in understanding the early failure of the alloy containing higher iron content levels. The 3D study along with fractography suggests that the failure occurring in these alloys is not only due to the brittleness of intermetallic particles, but also mainly due to the morphology of the intermetallic particles in the alloy. Therefore, methodologies to modify the intermetallic particles could help improve the mechanical properties of Al-Si recycled alloys.

CONCLUSION

- Al-7 Si alloys with two different levels of iron content, such as 0.6% and 2% Fe, were prepared using the casting method to study the effect of iron on the microstructure and mechanical properties of these alloys.
- Microstructural studies clearly show that the increase in iron content from 0.6% to 2% resulted in an increase in the average size, thickness and volume fraction of iron intermetallics in the alloy.
- Nano-indentation study shows that the hardness and Young's modulus of iron intermetallics (9.53 GPa and 174.30 GPa) are far more than those of primary aluminium (1.05 GPa and 102.78 GPa). Furthermore, the iron intermetallics are very brittle compared with the primary aluminium.
- Tensile test results show the deleterious effect of higher iron content on the mechanical properties

of Al-7Si alloys. The Al-7Si-0.6Fe alloy has a $\sim 10\%$ increase in elongation, while the strength of the alloy decreased by 6%. Increasing the iron content from 0.6% to 2% (Al-7Si-2Fe alloy) resulted in a reduction in elongation and strength by $\sim 58\%$ and 25%, respectively.

- 3D XCT study shows that the fracture occurred in a region where more intermetallic particles were found in the alloy. Also, careful observation of the fracture surface along with the XCT reconstructed image shows that the fracture of brittle intermetallic particles is not the reason for early failure of high-iron containing alloys during tensile loading, but the morphology and debonding of the particles and matrix at the interface are the reasons for failure of the alloy.
- The higher the iron content in the Al-7%Si alloy is, the higher the number of intermetallics, the bigger the platelet boundaries and the higher the tendency to crack propagation and early failure of the alloy.

OPEN ACCESS

This article is distributed under the terms of the Creative Commons Attribution 4.0 International License (<http://creativecommons.org/licenses/by/4.0/>), which permits unrestricted use, distribution, and reproduction in any medium, provided you give appropriate credit to the original author(s) and the source, provide a link to the Creative Commons license, and indicate if changes were made.

REFERENCES

1. G. Gaustad, E. Olivetti, and R. Kirchain, *Resour. Conserv. Recycl.* 58, 79 (2012).
2. C.B. Basak and N. Hari Babu, *Mater. Des.* 108, 277 (2016).
3. W. Khalifa, F.H. Samuel, and J.E. Gruzleski, *Metall. Mater. Trans. A Phys. Metall. Mater. Sci.* 34, 807 (2003).
4. J.A. Taylor, *Procedia Mater. Sci.* 1, 19 (2012).
5. S.J. Maggs, *Intermetallic Phase Selection in Dilute Al-Fe-Si Alloys* (1996). http://etheses.whiterose.ac.uk/4711/1/uk_bl_ethos_394317.pdf. Accessed 22 Oct 2018.
6. C.M. Dinnis, J.A. Taylor, and A.K. Dahle, *Scr. Mater.* 53, 955 (2005).
7. A. Couture, *Int. Cast Met. J.* 6, 9 (1981).
8. S.G. Shabestari, *Mater. Sci. Eng., A* 383, 289 (2004).
9. S.G. Shabestari, M. Mahmudi, M. Emamy, and J. Campbell, *Int. J. Cast Met. Res.* 15, 17 (2002).
10. F. Wang, Z. Zhang, Y. Ma, and Y. Jin, *Mater. Lett.* 58, 2442 (2004).
11. C.L. Chen, A. Richter, and R.C. Thomson, *Intermetallics* 17, 634 (2009).
12. W.C. Oliver and G.M. Pharr, *J. Mater. Res.* 19, 3 (2004).
13. J. Mathew, A. Mandal, S.D. Kumar, S. Bajpai, M. Chakraborty, G.D. West, and P. Srirangam, *J. Alloys Compd.* 712, 460 (2017).
14. K.M. Mussert, *J. Mater. Sci.* 37, 789 (2002).
15. E. Frutos, R. Martínez-Morillas, J.L. González-Carrasco, and N. Vilaboa, *Intermetallics* 19, 260 (2011).
16. ASTM Int., *Astm* (2009), pp. 1–27. <http://www.astm.org/Standards/E8.htm>.
17. S. Shankar, Y.W. Riddle, and M.M. Makhlof, *Acta Mater.* 52, 4447 (2004).
18. J.A. Taylor, G.B. Schaffer, and D.H. Stjohn, *Metall. Mater. Trans. A* 30, 1657 (1999).
19. S. Hegde and K.N. Prabhu, *J. Mater. Sci.* 43, 3009 (2008).

20. W.C. Oliver and G.M. Pharr, *J. Mater. Res.* 7, 1564 (1992).
21. E. Frutos, D.G. Morris, and M.A. Muñoz-Morris, *Intermetallics* 38, 1 (2013).
22. M. Zamanzade, H. Vehoff, and A. Barnoush, *Intermetallics* 41, 28 (2013).
23. S.W. Youn, P.K. Seo, and C.G. Kang, *J. Mater. Process. Technol.* 162, 260 (2005).
24. L.A. Narayanan, F.H. Samuel, and J.E. Gruzleski, *Metall. Mater. Trans. A* 25, 761 (1994).
25. M.F. Ibrahim, S.A. Alkahtani, K.A. Abuhasel, and F.H. Samuel, *Mater. Des.* 86, 30 (2015).
26. M. Sacinti, E. Cubuklusu, and Y. Birol, *Int. J. Cast Met. Res.* 30, 96 (2017).
27. M. Ravi, U.T.S. Pillai, B.C. Pai, A.D. Damodaran, and E.S. Dwarakadasa, *Int. J. Cast Met. Res.* 11, 113 (1998).
28. J.Z. Yi, Y.X. Gao, P.D. Lee, and T.C. Lindley, *Mater. Sci. Eng. A* 386, 396 (2004).
29. K. Gall, N. Yang, M. Horstemeyer, D.L. McDowell, and J. Fan, *Metall. Mater. Trans. A Phys. Metall. Mater. Sci.* 30, 3079 (1999).

Publisher's Note Springer Nature remains neutral with regard to jurisdictional claims in published maps and institutional affiliations.